

Fig. 7. Unknown vehicle reconstructed from the first (a) two, (b) three, (c) four, and (d) five silhouettes, second experiment.

## V. CONCLUSION

A simple algorithm for matching three-dimensional objects is proposed. It is based upon the use of the observed silhouettes of the unknown object. Experiments conducted show that as silhouettes are added to modify the three-dimensional structure of the unknown object, a consistent matching results from moments and Fourier transform coefficients. The speed of convergence depends on the amount of information supplied by the sequence of silhouettes, since small modification to the three-dimensional structure is made if a silhouette with little new information is added. From the experiments above, it is clear that for man-made objects with clearly defined faces and edges, a fast convergence is achieved if the principal or orthogonal silhouettes are observed. This technique fails when pieces of the object are missing or the object is not isolated, since the principal direction calculation will not be accurate.

## REFERENCES

- [1] L. T. Watson and L. G. Shapiro, "Identification of space curves from two-dimensional perspective views," *IEEE Trans. Pattern Anal. Machine Intell.*, vol. PAMI-4, pp. 469-475, Sept. 1982.
- [2] I. Chakravarty, "The use of characteristic views as a basis for recognition of three-dimensional objects," Rensselaer Polytechnic Institute, Troy, NY, Tech. Rep. IPL-TR-034, Oct. 1982.
- [3] W. N. Martin and J. K. Aggarwal, "Occluding contours in dynamic scenes," in *Proc. Conf. Pattern Recognition Image Processing*, Aug. 1981, pp. 189-192.
- [4] —, "Volumetric description of objects from multiple views," *IEEE Trans. Pattern Anal. Machine Intell.*, vol. PAMI-5, pp. 150-158, Mar. 1983.
- [5] Workshop on Representation Three-Dimensional Objects, Univ. Pennsylvania, Philadelphia, PA, May 1-2, 1979.
- [6] P. W. Likins, *Elements of Engineering Mechanics*. New York: McGraw-Hill, 1973.
- [7] C. T. Zahn and R. Z. Roskies, "Fourier descriptors for plane closed curves," *IEEE Trans. Comput.*, vol. C-21, pp. 269-281, Mar. 1971.
- [8] G. H. Granlund, "Fourier preprocessing for hand print character recognition," *IEEE Trans. Comput.*, vol. C-21, pp. 195-201, 1972.
- [9] E. Persoon and K. S. Fu, "Shape discrimination using Fourier descriptors," *IEEE Trans. Syst. Man Cybern.*, vol. SMC-7, pp. 170-179, 1977.
- [10] C. W. Richard and H. Hemami, "Identification of three-dimensional objects using Fourier descriptors of the boundary curve," *IEEE Trans. Syst. Man Cybern.*, vol. SMC-4, pp. 371-378, July 1974.
- [11] T. P. Wallace and O. R. Mitchell, "Analysis of three-dimensional movement using Fourier descriptor," *IEEE Trans. Pattern Anal. Machine Intell.*, vol. PAMI-2, pp. 583-588, Nov. 1980.

## Multiple Resolution Texture Analysis and Classification

SHMUEL PELEG, JOSEPH NAOR, RALPH HARTLEY, AND DAVID AVNIR

**Abstract**—Textures are classified based on the change in their properties with changing resolution. The area of the gray level surface is mea-

Manuscript received August 8, 1983; revised February 6, 1984. This work was supported by the Central Research Foundation of Hebrew University, and by the National Science Foundation under Grant MCS-82-18408.

S. Peleg was with the Center for Automation Research, University of Maryland, College Park, MD 20742. He is now with the Department of Computer Science, the Hebrew University of Jerusalem, 91904 Jerusalem, Israel.

J. Naor is with the Department of Computer Science, the Hebrew University of Jerusalem, 91904 Jerusalem, Israel.

R. Hartley is with the Center for Automation Research, University of Maryland, College Park, MD 20742.

D. Avnir is with the Department of Organic Chemistry, the Hebrew University of Jerusalem, 91904 Jerusalem, Israel.

sured at several resolutions. This area decreases at coarser resolutions since fine details that contribute to the area disappear. Fractal properties of the picture are computed from the rate of this decrease in area, and are used for texture comparison and classification. The relation of a texture picture to its negative, and directional properties, are also discussed.

**Index Terms**—Fractals, fractal signature, multiresolution methods, texture classification.

I. INTRODUCTION

The study of changes in picture properties resulting from changes in scale has been accelerated by Mandelbrot's work on fractals [4], [5]. A theoretical fractal object is self-similar under all magnifications, and property changes when undergoing scale changes are limited; doubling resolution, for example, will always yield an identical change, regardless of the initial scale.

One of the important properties of fractal objects is their surface area. For pictures, the area of the gray level surface has been measured at different scales. The change in measured area with changing scale was used as the "fractal signature" of the texture, and signatures were compared for texture classification. Treating the areas of the upper side and lower side of the gray level surface separately resulted in interesting variations on this method. These variations, along with the method used for scale change, are discussed in the following sections.

Earlier results on texture analysis using fractal techniques are reported by Nguyen and Quinqueton [9] and Pentland [6]. While Nguyen and Quinqueton use only one-dimensional fractal analysis along a space filling curve, Pentland performs full two-dimensional analysis. Pentland used statistics of differences of gray levels between pairs of pixels at varying distances as indicators of the fractal properties of the texture. Under the assumption that textures are fractals for a certain range of magnifications, he obtained good classification results based on the computed fractal dimension. Related work on multiresolution texture analysis using pyramids is reported by Larkin and Burt [2], and general discussion on texture analysis can be found in [3], [7], [8]. The texture pictures in this correspondence were taken from Brodatz [1].

II. THE AREA OF THE GRAY LEVEL SURFACE

Measuring the area of the gray level surface is based on methods suggested by Mandelbrot [5] for curve length measurements.

A. Measuring Curve Length

The following methods are described by Mandelbrot for measuring the lengths of irregular coastlines.

1) Given a yardstick of length  $\epsilon$ , walk the yardstick along the coastline. The number of steps multiplied by  $\epsilon$  is an approximate length  $L(\epsilon)$  of the coastline. For a coastline, when  $\epsilon$  becomes smaller, the observed length  $L(\epsilon)$  increases without limit. This method is based on approximating the curve with a polygon made from segments of length  $\epsilon$ .

2) The shortest path on the land that is not further than  $\epsilon$  from the water can be regarded as an approximate length  $L(\epsilon)$  of the coastline. This method discriminates between land and water—a property Mandelbrot found undesirable. However, this discrimination between sides of curves or surfaces will be found to be useful for some texture properties.

3) Consider all points with distances to the coastline of no more than  $\epsilon$ . These points form a strip of width  $2\epsilon$ , and the suggested length  $L(\epsilon)$  of the coast is the area of the strip divided by  $2\epsilon$ . Here, too, as  $\epsilon$  decreases  $L(\epsilon)$  increases.

4) Cover the coastline with the minimal number of disks of radius  $\epsilon$ , not necessarily centered on the coastline as in c). Let  $L(\epsilon)$  be the total area of these disks divided by  $2\epsilon$ .

Mandelbrot reports studies that show that for many coastlines

$$L(\epsilon) \approx F\epsilon^{1-D} \tag{1}$$

where  $F$  and  $D$  are constants for the specific coastline. He called  $D$  the "fractal dimension" of the line. Note that for a straight line  $D = 1$ , and  $F$  is the true length of the line. For fractal curves,  $D$  is independent of  $\epsilon$ , and when one plots  $L(\epsilon)$  versus  $\epsilon$  on log-log scale one gets a straight line with slope  $1 - D$ . When  $D$  varies with  $\epsilon$  and is not a constant, the above plot will not be a straight line.

B. Measuring Surface Area

To compute the surface area, approach c) above was adopted, as its surface extension seems to be computationally efficient. In this extension from curve to surface, all points in the three-dimensional space at distance  $\epsilon$  from the surface were considered, covering the surface with a "blanket" of thickness  $2\epsilon$ . The surface area is then the volume occupied by the blanket divided by  $2\epsilon$ . The covering blanket is defined by its upper surface  $u_\epsilon$  and its lower surface  $b_\epsilon$ . Initially, given the gray level function  $g(i, j)$ ,  $u_0(i, j) = b_0(i, j) = g(i, j)$ . For  $\epsilon = 1, 2, 3, \dots$ , the blanket surfaces are defined as follows:

$$u_\epsilon(i, j) = \max \left\{ u_{\epsilon-1}(i, j) + 1, \max_{|(m, n) - (i, j)| \leq 1} u_{\epsilon-1}(m, n) \right\} \tag{2}$$

and

$$b_\epsilon(i, j) = \min \left\{ b_{\epsilon-1}(i, j) - 1, \min_{|(m, n) - (i, j)| \leq 1} b_{\epsilon-1}(m, n) \right\}. \tag{3}$$

The image points  $(m, n)$  with distance less than one from  $(i, j)$  were taken to be the four immediate neighbors of  $(i, j)$ . Similar expressions exist when the eight-neighborhood is desired. A point  $(x, y, f)$  will be included in the blanket for  $\epsilon$  when  $b_\epsilon(x, y) < f \leq u_\epsilon(x, y)$ . The blanket definition uses the fact that the blanket of the surface for radius  $\epsilon$  includes all the points of the blanket for radius  $\epsilon - 1$ , together with all the points within radius 1 from the surfaces of that blanket. Expression (2), for example, ensures that the new upper surface  $u_\epsilon$  is higher by at least 1 from  $u_{\epsilon-1}$ , and also at distance at least 1 from  $u_{\epsilon-1}$  in the horizontal and vertical directions.

The volume of the blanket is computed from  $u_\epsilon$  and  $b_\epsilon$  by

$$v_\epsilon = \sum_{i, j} (u_\epsilon(i, j) - b_\epsilon(i, j)). \tag{4}$$

A one-dimensional illustration of the expansion process is shown in Fig. 1.

As the surface area measured with radius  $\epsilon$  we take the volume of the added layer from radius  $\epsilon - 1$ , divided by 2 to account for both the upper and lower layers:

$$A(\epsilon) = \frac{(v_\epsilon - v_{\epsilon-1})}{2}. \tag{5}$$

This definition deviates from the original method in Section II-A, which suggests that surface area be taken as  $v_\epsilon/2\epsilon$ . This is necessary, since  $v_\epsilon$  depends on all smaller scales features. Subtracting  $v_{\epsilon-1}$  isolates just those features that change from scale  $\epsilon - 1$  to scale  $\epsilon$ . When a pure fractal object is analyzed, both definitions are identical since property changes are independent on scale, and measurements between any two different scales will yield the same fractal dimension. However, for nonfractal objects this isolation from the effects of smaller scale features is necessary. Definition (5) gives reasonable measures for both fractal and nonfractal surfaces.

The area of a fractal surface behaves according to the expression (Mandelbrot [5]):

$$A(\epsilon) = F\epsilon^{2-D}.$$

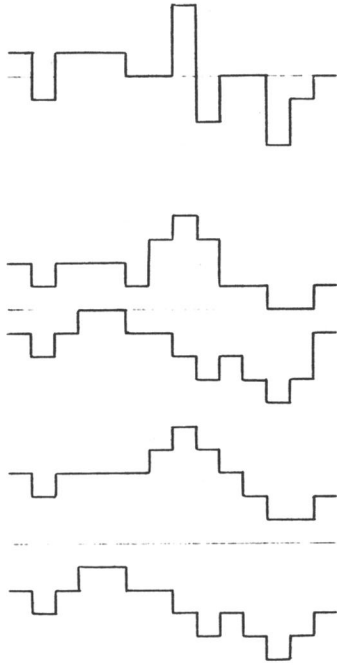


Fig. 1. A one-dimensional function  $g$  and its covering blanket for  $\epsilon = 1, 2$ . The blanket volumes (areas) are  $v(1) = 47$  and  $v(2) = 78$ . The respective measured lengths are  $L(1) = (47-0)/2 = 23.5$  and  $L(2) = (78-47)/2 = 15.5$ .

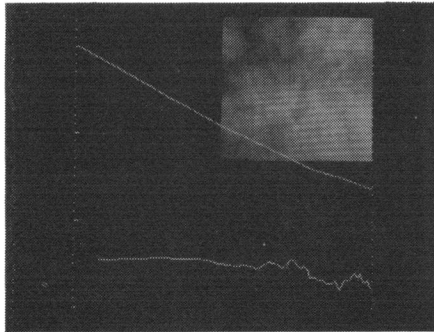


Fig. 2. A fractal picture generated by a Brownian process. The plot of its measured surface area,  $A(\epsilon)$  versus  $\epsilon$  in a log-log scale, is the top curve. The fractal signature in the bottom curve is the slope  $S(\epsilon)$  of  $A(\epsilon)$ . The average slope of  $A(\epsilon)$  is 0.51, giving an observed fractal dimension of 2.51. This result matches well the theoretical dimension of 2.5 computed by Mandelbrot.

When plotting  $A(\epsilon)$  versus  $\epsilon$  on a log-log scale, one gets a straight line of slope  $2-D$ . This curve does not have to be straight for nonfractal surfaces. The slope of  $A(\epsilon)$  on the log-log scale is of great interest, and for each gray level surface a "fractal signature"  $S(\epsilon)$  is computed for each  $\epsilon$  by finding the slope of the best fitting straight line through the three points  $(\log(\epsilon - 1), \log(A(\epsilon - 1)))$ ,  $(\log(\epsilon), \log(A(\epsilon)))$ , and  $(\log(\epsilon + 1), \log(A(\epsilon + 1)))$ . For fractal objects  $S(\epsilon)$  should be equal to  $2-D$  for all  $\epsilon$ .

To test our definitions, we constructed a fractal surface as suggested by Mandelbrot [5]: a line was randomly placed over a plane dividing it into two half-planes. An arbitrarily chosen half-plane was elevated by 1. This process was iterated many times, and for the  $k$ th iteration the added elevation was  $1/\sqrt{k}$ . The resulting matrix was linearly transformed into the picture limits. Fig. 2 shows the resulting picture after 1000 iterations, together with the area function  $A(\epsilon)$  and the fractal signature  $S(\epsilon)$ . As predicted,  $A(\epsilon)$  is a straight line, and  $S(\epsilon)$  is almost a constant at the value 0.51 giving a measured fractal dimension of 2.51. This value is very close to the theoretical fractal dimension of  $5/2$  as given by Mandelbrot.

### III. TEXTURE ANALYSIS AND CLASSIFICATION

The magnitude of the fractal signature  $S(\epsilon)$  relates to the amount of detail that is lost when the size of the measuring yardstick passes  $\epsilon$ . High values of  $S(\epsilon)$  relate to strong gray level variations at distance  $\epsilon$ . High values at small  $\epsilon$  result from significant "high-frequency" gray level variations, while high values for larger  $\epsilon$  result from significant "low-frequency" variations. Thus, the fractal signature  $S(\epsilon)$  gives important information about the fineness of the variations of the gray level surface, with no need for artificial decomposition into harmonic frequencies as is done in Fourier analysis.

The fractal signatures have been computed for several texture pictures of size  $128 \times 128$ , and are displayed in Fig. 3. For two samples of every texture the surface area  $A(\epsilon)$  (for  $\epsilon = 1, 2, \dots, 50$ ) and the fractal signature  $S(\epsilon)$  (for  $\epsilon = 2, 3, \dots, 49$ ) are displayed.

Textures are compared based on the differences between their fractal signatures. For two textures  $i$  and  $j$  with signatures  $S_i$  and  $S_j$  the distance is defined by

$$D(i, j) = \sum_{\epsilon} (S_i(\epsilon) - S_j(\epsilon))^2 \log \left( \frac{\epsilon + \frac{1}{2}}{\epsilon - \frac{1}{2}} \right). \quad (6)$$

The weighting by  $\log [(\epsilon + \frac{1}{2})/(\epsilon - \frac{1}{2})]$  is due to the unequal spacing of the points in the log-log scale. These distances are shown in Table I between all pairs of texture pictures tested. A texture is identified with the closest signature, giving almost perfect results for the tested images. The relative attractiveness of these results is based on the relatively small number of texture descriptors. While only 48 features were used in our experiments, corresponding to  $S(\epsilon)$  for  $\epsilon = 2, \dots, 49$ , this number can vary according to texture properties.

### IV. SYMMETRY ISSUES

When describing method b) for coastline measurement (Section II-A), Mandelbrot [5] criticizes it as being discriminatory between land and water; i.e., when reversing the role of land and water different length measurements might result. However, these very differences can reveal some important properties of the curve (or surface). Fig. 4 exhibits this asymmetry in length measurements.

Consider, for example, an image of light particles scattered over a dark background. When high gray level stands for white, the min operator of (3) will shrink the light regions corresponding to the particles, and the rate of this shrinking will only depend on the shape properties of the particles. The max operator of (2), however, will shrink the background regions, and the rate of this shrinking will mainly be affected by the distribution of the particles.

To take advantage of this asymmetry, we divide our surface area measurements into two parts: measuring the area of the gray level surface when viewing it from "above" and measuring the area when viewing the surface from "below." We change the volume definition of (4) to the following two definitions of "upper volume"  $v^+$  and "lower volume"  $v^-$  as follows:

$$v_{\epsilon}^+ = \sum_{i,j} (u_{\epsilon}(i, j) - g(i, j)) \quad (7a)$$

and

$$v_{\epsilon}^- = \sum_{i,j} (g(i, j) - b_{\epsilon}(i, j)). \quad (7b)$$

The area expression (5) is also changed into "top area"  $A^+$  and "bottom area"  $A^-$  as follows:

$$A^+(\epsilon) = v_{\epsilon}^+ - v_{\epsilon-1}^+ \quad (8a)$$

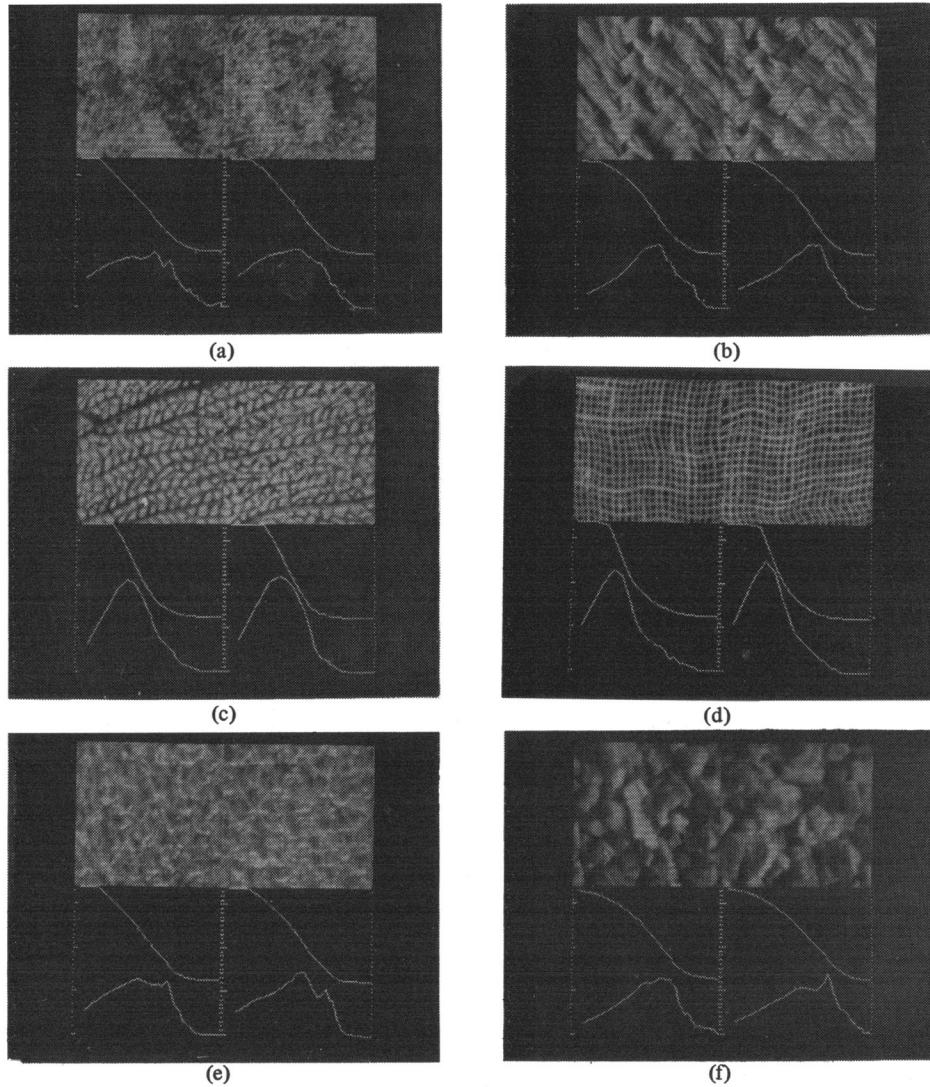


Fig. 3. Textures studied (two samples each), with plots of their associated areas  $A(\epsilon)$  on a log-log scale (upper curve), and the fractal signatures  $S(\epsilon)$  (lower curve). (a) Ice. (b) Raffia. (c) Seafan. (d) Burlap. (e) Pigskin. (f) Mica.

TABLE I  
DIFFERENCES BETWEEN ALL PAIRS OF TEXTURE PICTURES, AS DEFINED IN (6). MINIMAL DIFFERENCES FOR EVERY COLUMN ARE UNDERLINED. ONLY ONE MISCLASSIFICATION OCCURS, BETWEEN *pig1* and *ice1*.

	seafan1	seafan2	burlap1	burlap2	ice1	ice2	pig1	pig2	raffia1	raffia2	mical	mica2
seafan1	0.000	<u>0.013</u>	0.114	0.168	0.218	0.143	0.214	0.255	0.359	0.353	0.518	0.513
seafan2	<u>0.013</u>	0.000	0.101	0.135	0.311	0.217	0.315	0.354	0.520	0.488	0.573	0.555
burlap1	0.114	0.101	0.000	<u>0.012</u>	0.354	0.283	0.405	0.477	0.683	0.613	0.507	0.778
burlap2	0.168	0.135	<u>0.012</u>	0.000	0.499	0.400	0.545	0.625	0.852	0.783	1.000	0.958
ice1	0.218	0.311	0.354	0.499	0.000	<u>0.013</u>	<u>0.011</u>	0.023	0.055	0.045	0.105	0.100
ice2	0.143	0.217	0.283	0.400	0.013	0.000	0.018	0.033	0.101	0.073	0.154	0.171
pig1	0.214	0.315	0.405	0.545	0.011	0.018	0.000	<u>0.013</u>	0.048	0.029	0.083	0.084
pig2	0.255	0.354	0.479	0.625	0.023	0.033	0.013	0.000	0.035	0.024	0.070	0.079
raffia1	0.359	0.520	0.683	0.852	0.068	0.101	0.048	0.035	0.000	<u>0.010</u>	0.028	0.042
raffia2	0.353	0.488	0.613	0.783	0.045	0.073	0.029	0.024	<u>0.010</u>	0.000	0.034	0.053
mical	0.518	0.573	0.507	1.000	0.105	0.164	0.083	0.070	0.028	0.034	0.000	<u>0.009</u>
mica2	0.513	0.555	0.778	0.958	0.100	0.171	0.084	0.079	0.042	0.053	<u>0.009</u>	0.000

$$A^-(\epsilon) = v_{\epsilon}^- - v_{\epsilon-1}^- \tag{8b}$$

Two different fractal signatures  $S^+$  and  $S^-$  are also computed.

Fig. 5 displays two collections of parts, together with their top and bottom fractal signature graphs. As expected, the  $S^-$

graphs, representing the shapes of the parts, are identical for both pictures, while the  $S^+$  graphs, representing the background, are different. The textures of Fig. 3 were analyzed again, this time differentiating between top areas and bottom areas, and the distance between two textures  $i$  and  $j$  was defined as

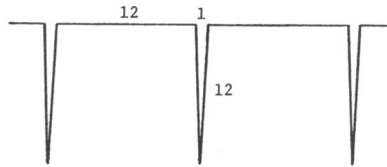


Fig. 4. Nonsymmetric length measurement for a curve. For  $\epsilon \ll 1$ , measured length will be approximately 102 regardless of side. Measuring the length from above, the curve will look like a straight line and have a measured length of about 33 for  $\epsilon > 1$ , as the narrow cracks will not be measurable. Measuring the length from below, the curve will behave as a straight line only for  $\epsilon > 12$ .

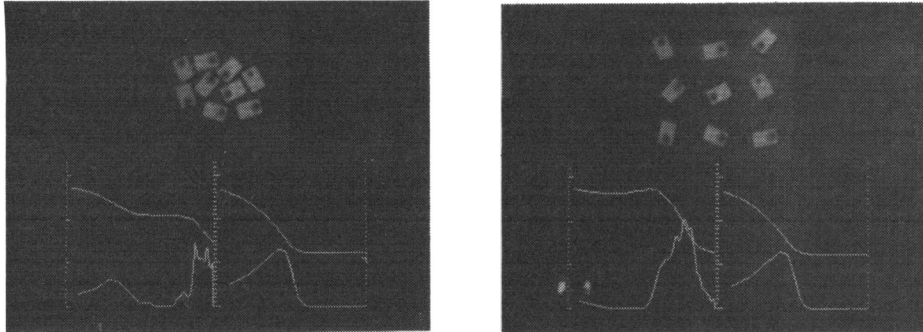


Fig. 5. Parts spread in two different configurations. In both pictures,  $A(\epsilon)$  and  $S(\epsilon)$  for the bottom area (right side of each photo), which correspond to the parts' shape, behave identically. The top area (left side of each photo), which corresponds to the shape of the background, behaves extremely differently.

TABLE II  
DIFFERENCES BETWEEN ALL PAIRS OF TEXTURE PICTURES AS DEFINED IN (9),  
WHEN UPPER AND LOWER SIDES OF THE GRAY LEVEL SURFACE ARE  
EXAMINED SEPARATELY. ALL TEXTURES ARE CLASSIFIED CORRECTLY.

	seafan1	seafan2	burlap1	burlap2	ice1	ice2	pig1	pig2	raffa1	raffa2	mica1	mica2
seafan1	0.000	0.071	0.400	0.544	0.529	0.355	0.659	0.683	0.865	0.818	1.230	1.178
seafan2	0.071	0.000	0.391	0.439	0.703	0.478	0.768	0.884	1.124	1.076	1.472	1.438
burlap1	0.400	0.391	0.000	0.042	0.850	0.668	0.819	0.907	1.401	1.326	1.598	1.577
burlap2	0.544	0.439	0.042	0.000	1.089	0.914	1.076	1.227	1.875	1.656	1.959	1.941
ice1	0.529	0.703	0.850	1.089	0.000	0.018	0.089	0.101	0.150	0.112	0.272	0.257
ice2	0.355	0.478	0.668	0.914	0.018	0.000	0.161	0.179	0.227	0.185	0.413	0.427
pig1	0.659	0.768	0.819	1.076	0.089	0.161	0.000	0.035	0.204	0.150	0.170	0.213
pig2	0.683	0.884	0.907	1.227	0.101	0.179	0.035	0.000	0.157	0.115	0.151	0.175
raffa1	0.865	1.124	1.401	1.835	0.150	0.227	0.204	0.157	0.000	0.025	0.140	0.124
raffa2	0.818	1.076	1.326	1.656	0.112	0.185	0.150	0.115	0.025	0.000	0.147	0.139
mica1	1.230	1.472	1.598	1.959	0.272	0.413	0.170	0.151	0.140	0.147	0.000	0.033
mica2	1.178	1.438	1.577	1.941	0.257	0.427	0.213	0.175	0.124	0.139	0.033	0.000

$$D'(i, j) = \sum_{\epsilon} \left\{ [(S_i^+(\epsilon) - S_j^+(\epsilon))^2 + (S_i^-(\epsilon) - S_j^-(\epsilon))^2] \cdot \log \left( \frac{\epsilon + \frac{1}{2}}{\epsilon - \frac{1}{2}} \right) \right\} \quad (9)$$

The distance as defined above is shown in Table II. This time, the classification results are all correct.

#### V. DIRECTIONAL PROPERTIES

All methods described so far are invariant to texture direction. When directionality of the texture is of importance, the blanket growth in (2) and (3) could be made directional. Maximizing (or minimizing) in a circular neighborhood can be replaced by a nonsymmetric neighborhood. Directional analysis of the Brodatz "raffa" texture is displayed in Fig. 6. In this

case, the neighborhood consisting of the four immediate neighbors has been replaced by the following choices: 1) upper and lower neighbors; 2) left and right neighbors; 3) upper-left and lower-right diagonal neighbors; 4) upper-right and lower-left diagonal neighbors. The differences in the fractal signatures reveal the directional characteristics of the "raffa" texture.

#### VI. CONCLUDING REMARKS

An approach to analysis and classification of textures is described, based on scale varying surface area measurements as suggested by Mandelbrot for fractal objects. Although textures are mostly not fractal for the entire scale range, the change in these measurements proved to be helpful in characterizing the texture. "Frequency" information about texture can be obtained directly in the spatial domain without need to use the

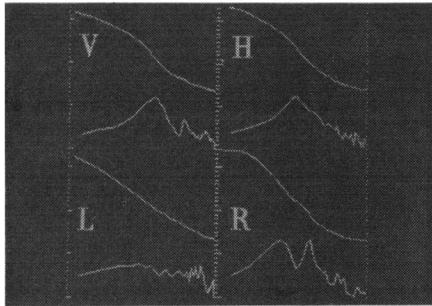


Fig. 6. Directional analysis of "raffia" exhibits similar properties for the vertical (*V*) and horizontal (*H*) directions, but different properties for the diagonal directions.

frequency domain. As with almost any multiresolution approach, efficient implementation in pyramid data structures should be studied.

Applications of fractal analysis to textural problems of materials of industrial importance (e.g. adsorbents, catalysts) as well as comparison of this technique to surface-texture probing by absorption experiments [10], [11] are in progress.

#### REFERENCES

- [1] P. Brodatz, *Textures: A Photographic Album for Artists and Designers*. Dover, 1966.
- [2] L. I. Larkin and P. J. Burt, "Multi-resolution texture energy measures," in *Proc. IEEE Comput. Soc. Conf. Comput. Vision Pattern Recognition*, Washington, DC, June 1983, pp. 519-520.
- [3] K. Laws, "Textured image segmentation," USC Image Processing Inst., Rep. 940, 1980.
- [4] B. B. Mandelbrot, *Fractals: Form, Chance and Dimension*. San Francisco, CA: Freeman, 1977.
- [5] —, *The Fractal Geometry of Nature*. San Francisco, CA: Freeman, 1982.
- [6] A. Pentland, "Fractal-based description of natural scenes," in *Proc. IEEE Comput. Soc. Conf. Comput. Vision Pattern Recognition*, Washington, DC, June 1983, pp. 201-209.
- [7] W. K. Pratt, O. D. Faugeras, and A. Galalowicz, "Applications of stochastic texture fields models to image processing," *Proc. IEEE*, May 1981.
- [8] R. M. Haralick, K. Shanmugam, and I. Dinstein, "Texture features for image classifications," *IEEE Trans. Syst. Man Cybern.*, vol. SMC-3 pp. 610-622, Nov. 1973.
- [9] P. T. Nguyen and J. Quinqueton, "Space filling curves and texture analysis," in *Proc. 6th Int. Conf. Pattern Recognition*, Munich, Germany, 1982, pp. 282-285.
- [10] D. Avnir and P. Pfeifer, "Fractal dimension in chemistry: An intensive characteristic of surface irregularity," *Nouv. J. Chim.*, vol. 7, pp. 71-72, 1983.
- [11] P. Pfeifer, D. Avnir, and D. Farin, "Ideally irregular surfaces of dimension greater than two, in theory and practice," *Surface Sci.*, vol. 126, pp. 569-572, 1983.

### Determining Motion Parameters for Scenes with Translation and Rotation

CHARLES JERIAN AND RAMESH JAIN

**Abstract**—A study of methods that determine the rotation parameters of a camera moving through synthetic and real scenes is conducted. Algorithms that combine ideas of Jain and Prazdny, using hypothesize-and-verify paradigm, are developed to find translational and rotational

parameters. An argument is made for using hypothesized motion parameters rather than relaxation labeling to find correspondence. Some work with real scenes shows the difficulties introduced by noise, the lack of resolution, and the need for better low-level techniques.

**Index Terms**—Dynamic scene analysis, focus of expansion, hypothesize, motion parameters, optical flow.

#### I. INTRODUCTION

There have been many different approaches to extracting the motion information from sequences of dynamic scenes [13], [18]–[20], [24], [29], [30]. A number of these methods concentrated on determining the FOE or focus of expansion form of the translational parameters. Most of these methods require optical flow vectors or corresponding points in different discrete frames as input. Other methods seek to use the focus of expansion to yield the correspondence [13]. The FOE as the intersection of all optical flow vectors does not exist when the system undergoes rotation, however we feel that the concept of a FOE can still be used in analyzing 3-dimensional motion parameters and in solving the correspondence problem for such cases [20]–[23].

Roach and Aggarwal [24] showed the sensitivity of nonlinear methods for the recovery of structure from motion to the noise in location of tokens. Tsai and Huang [25]–[27] proposed a linear method, assuming correspondence of eight points in two frames, for the recovery of motion parameters. This mathematically elegant method is very sensitive to noise in the location of the points. It is possible to develop, however, a *hypothesize-and-verify* approach to recover motion parameters using this approach. In this correspondence, we present some of our studies using optimization and linear methods for the recovery of motion parameters using the hypothesize-and-verify paradigm. This will allow better recovery using the existing approaches. Based on the experiments we did, it appears that none of the existing methods is robust enough to function independently in real images. This encouraged us to study the feasibility of combining features of different approaches and develop a paradigm for the recovery in real scenes. We discuss problems of locating features and their effect on the recovery.

#### II. RECOVERY OF 3-D MOTION PARAMETERS

One simple method for determining the focus of expansion in scenes where corner points or other matchable entities have been extracted has been proposed by Jain [9]. This method does not use a correspondence between the frames, rather it uses the triangle inequality to show that in approaching motion the sum of the distances of points in the second frame from the FOE minus the sum of the distances of points in the first frame from the FOE is maximized. This method is difficult to apply directly to real scenes because most corner detectors can lose points from frame to frame and can also find multiple points in both frames. However, the idea of hypothesizing a likely focus of expansion and verifying it in some way against the image is an important method. In this correspondence we will suggest other variations of this basic hypothesize-and-verify paradigm. In Prazdny's work also, optimization of a quality of fit function was proposed to find the rotation parameters from given optic flow vectors and this was tested on synthetic data [22].

As an alternative to this method a linear solution to rotation and translation parameters have been found by Tsai and Huang [25]–[28]. Tsai and Huang have a linear algorithm for finding the direction of motion and the rotation parameters given optical flow. Their method is in contrast to the optimization methods in that it uses a system of linear equations. All other systems studied have nonlinear equations in their methods.

Manuscript received March 10, 1983; revised October 7, 1983.

The authors are with the Department of Electrical and Computer Engineering, University of Michigan, Ann Arbor, MI 48109.